CHEMISTRY OF MATERIALS
Cite This: Chem. Mater. 2019, 31, 4831−4839
Article
pubs.acs.org/cm

Controlling Size, Defectiveness, and Fluorescence in Nanoparticle UiO-66 through Water and Ligand Modulation

Gerald E. Decker,[†,§] Zachary Stillman,[‡,§] Lucas Attia,[‡] Catherine A. Fromen,*[,‡] and Eric D. Bloch*[,†]

[†]Department of Chemistry and Biochemistry and [‡]Department of Chemical and Biomolecular Engineering, University of Delaware, Newark, Delaware 19716, United States

Supporting Information

ABSTRACT: UiO-66, a zirconium(IV) metal−organic framework composed of six-metal clusters and terephthalic acid ligands, displays excellent thermal and chemical stability and has functions in gas storage, catalysis, selective adsorption, and drug delivery. Though the stability of UiO-66 is highly advantageous, simultaneous synthetic control over particle size and defectiveness of UiO-66 remains difficult to attain. Using an acid-free solvothermal synthesis, we demonstrate that particle size, defectiveness, and inherent fluorescence of UiO-66 can be precisely tuned using the molar ligand-to-metal ratio, quantified water content, and reaction time during synthesis. These three synthetic handles allow for reproducible modulation of UiO-66 defectiveness between 0 and 12% and particle size between 20 and 120 nm, while maintaining high crystallinity in the nanoparticles that were formed. We also find that particle defectiveness is linked to common overestimation of particle size measurements obtained via dynamic light scattering and propose a model to correct elevated hydrodynamic diameter measurements. Finally, we report inherent fluorescence of nonfunctionalized UiO-66, which exhibits peak fluorescence at a wavelength of 390 nm following excitation at 280 nm and is maximized in large, defect-free particles. Overall, this synthetic approach and characterization of defect, size, and fluorescence represent new opportunities to tune the physiochemical properties of UiO-66.

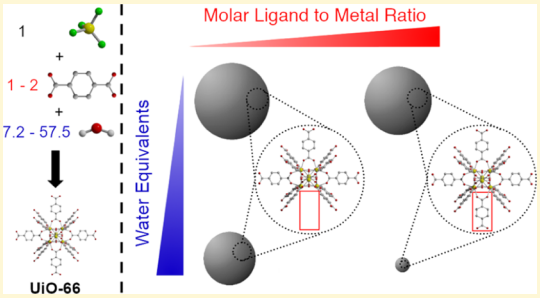

INTRODUCTION

Metal−organic frameworks (MOFs) have been widely investigated over the past decade for a variety of factors, including their record surface areas and tunable pore chemistry.[1−5] Uniquely to MOFs, these characteristics are possible because of the variety of structures and ligand functional groups that can be utilized to form these regular, structured frameworks. Accordingly, MOFs have many proposed applications including uses in gas storage and separation, catalysis, biomedicine, batteries, and sensors.[6−10] However, many reported MOFs lack the thermal or chemical stability needed to be compatible with large-scale implementation.[11] As many MOFs are based on divalent metal cations and carboxylic acid ligands, their relatively weak metal−ligand bonds typically afford materials with limited thermal, chemical, mechanical, and/or hydrolytic stability.[12−15] Higher stability materials typically feature higher valent metal cations or ligands with increased basicity, such as triazolate or pyrazolate groups.[16] In the case of the former, the UiO (University of Oslo) series of framework materials show considerable promise with greater thermal, chemical, and hydrolytic stability. Among these materials, the most widely studied has been the terephthalic acid-based MOF, UiO-66 (Figure 1).[17] This material, based on a six zirconium(IV) cluster, is well-known for both its high stability and amenability to postsynthetic modification strategies.[18,19]

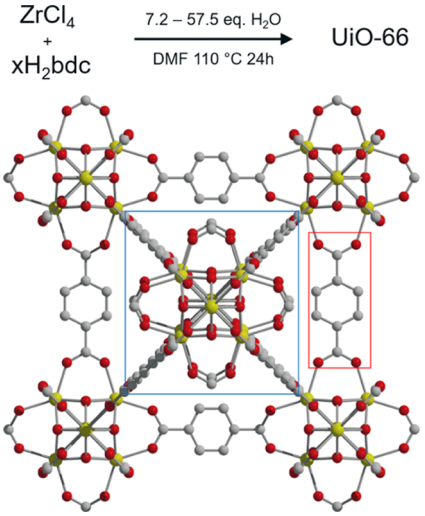

Figure 1. Reaction scheme of UiO-66. The blue box highlights the six-metal cluster, while the red box indicates a terephthalic acid ligand. The absence of the former is termed "cluster defective" and the latter "ligand defective".

Received: April 8, 2019
Revised: June 7, 2019
Published: June 10, 2019

DOI: 10.1021/acs.chemmater.9b01383
Chem. Mater. 2019, 31, 4831−4839

Although UiO-66 is nominally referred to as $Zr_6O_4(OH)_4(bdc)_6$ (bdc^{2-} = 1,4-benzenedicarboxylate), its composition is highly variable based on synthetic and activation conditions. The framework has a well-known dehydration step upon heating above 250 °C to afford $Zr_6O_6(bdc)_6$.[20] This transformation has a pronounced effect on material properties and has been leveraged to tune gas adsorption, ionic conductivity, and catalytic properties.[21] The preactivation composition of the structure is also highly variable.[22] In order to modulate the crystallinity of the product, acids are routinely added to UiO-66 syntheses.[23,24] The use of these compounds, which are often referred to as modulators and have included both mineral and organic acids, has also been found to profoundly affect the particle size. Reports of UiO-66 particle sizes range from 10 to over 1000 nm.[25,26] The inclusion of acid in MOF synthesis also plays an important role in material composition and reproducibility.[27] Depending on the exact synthetic conditions, UiO-66 is often produced with high levels of structural defects.[28] These defects, which can be attributed to either missing ligands or missing clusters in the structure, are closely tied to material properties including surface area, hydrolytic stability, and thermal stability.[29−31] Such characteristics can have immense effects on a material's usefulness in its intended application.[32] For example, higher defect UiO-66 displays higher gas adsorption capacities as compared to the defect-free material.[24] Currently, there are no synthetic approaches to simultaneously tune the extent of UiO-66 defectiveness and the resultant particle size, limiting the overall applicability of this MOF material.

As shown in Figure 1, the synthesis of UiO-66 typically proceeds via a solvothermal route by reacting $ZrCl_4$ and H_2bdc at elevated temperatures in appropriate nonanhydrous, amide-based solvents. The chosen solvent is frequently *N*,*N*-dimethylformamide (DMF), often with uncharacterized water content. Water is necessary for the formation of the $Zr_6O_4(OH)_4^{12+}$ cluster in UiO-66 and is thus required for material synthesis;[33] however, it has been demonstrated that high water content in the solvent can impede crystallization.[34] This has been the case both for syntheses in which water is the only modulator and for those using other modulators, such as acid.[35] Surprisingly, the role of water in UiO-66 synthesis remains poorly characterized, and its undocumented presence may contribute to the overall synthetic challenge of generating low-defect, chemically stable, UiO-66 nanoparticles of controlled size.

We sought to investigate the intricately coupled nature of particle size and defectiveness in UiO-66 as a function of water content and molar ligand-to-metal (L/M) ratio by utilizing acid-free syntheses. Herein, we use a combination of characterization techniques to unambiguously determine the size of low-defect and defect-free UiO-66 nanoparticle materials ranging in size from 20 to 120 nm. We demonstrate that particle size, defectiveness, and inherent fluorescence of UiO-66 can be precisely tuned using the L/M ratio, quantified water content, and reaction time during synthesis. Through our detailed analysis linking synthetic conditions to resultant UiO-66 structure−property relationships, we aim to provide a rational approach to the design of UiO-66 nanoparticles.

EXPERIMENTAL SECTION

Materials and Methods. All solid reagents were purchased from commercial vendors and used without further purification. DMF was obtained from a solvent purification system and stored in an amber bottle under 4 Å sieves. Powder X-ray diffraction (PXRD) measurements were collected on a Bruker D8 XRD (LynxEye position-sensitive detector) operating with a Cu Kα1 X-ray generator (λ = 1.54 Å) with a 40 kV beam voltage and 40 mA current. ^{1}H NMR spectra were taken on a Bruker AV 400 spectrometer. Low-pressure N_2 adsorption measurements were measured with 5.0 purity gas on a Micromeritics TriStar II Plus at 77 K in liquid nitrogen baths. Brunauer−Emmett−Teller (BET) surface areas were calculated as previously reported.[36] UV−vis measurements were carried out using an AvaSpec-ULS2048CL with a deuterium−halogen light source and a fiber-optic reflection probe. Infrared (IR) spectroscopy measurements were carried out using a Bruker ALPHA II.

Synthesis of UiO-66. For samples synthesized with a 1:1 L/M ratio, $ZrCl_4$ (90.0 mg, 0.386 mmol) and terephthalic acid (H_2bdc) (64.1 mg, 0.386 mmol) were dissolved in 15 mL of DMF along with a known amount of deionized H_2O relative to $ZrCl_4$ in a 20 mL vial. The same procedure is used for higher L/M ratios, maintaining 90 mg of $ZrCl_4$ and adding a larger mass of ligand to stoichiometrically increase the ratio. A total of 15 synthetic conditions were utilized for the study, as shown in Table 1. Once the solution was clear, it was then heated at 110 °C for 24 h. The sample was then centrifuged, the supernatant was decanted, and the isolated powder was soaked in DMF for 72 h, replacing the solvent every 24 h. This was followed by a similar washing procedure with MeOH, after which the solvated powder was dried under flowing N_2 before being loaded into a gas adsorption tube and heated under flowing N_2 for 48 h at 100 °C.

Table 1. Sample Key[a]

Water Eq. / L:M Ratio	7.2 eq. a, ★	14.4 eq. b, ■	28.7 eq. c, ●	43.1 eq. d, ▲	57.5 eq. e, ▼
1:1	1a (★)	1b (■)	1c (●)	1d (▲)	1e (▼)
1.5:1	1.5a (★)	1.5b (■)	1.5c (●)	1.5d (▲)	1.5e (▼)
2:1	2a (★)	2b (■)	2c (●)	2d (▲)	2e (▼)

[a]The table shows the labeling key used to denote the synthetic conditions used to synthesize each of the 15 samples studied. Symbols indicate water content, and colors represent L/M.

Kinetic Growth Study. Five different synthetic conditions of the aforementioned 15 were chosen for an in-depth kinetic growth study (1b red square, 1d red triangle, 1.5c black circle, 2b blue square, and 2d blue triangle). At each reaction condition, eight individual samples for each condition were synthesized to be removed at 15 min, 30 min, 1 h, 2 h, 4 h, 6 h, 12 h, and 24 h time points. Once the samples were removed from heat, they were flash-frozen with liquid nitrogen to 77 K to prevent further growth and stored at 195 K. Once all of the samples were synthesized, they were centrifuged down and decanted to remove any unreacted starting material. The remaining powder in the vials was dried without further washing to isolate the dry powder, which was used for defect testing as well as particle sizing.

Thermogravimetric Analysis. Thermal stability and oxygen defect testing thermogravimetric analyses (TGAs) were carried out using a TA Q5000 SA. For thermal stability studies, at least 10 mg of UiO-66 was loaded onto a tared aluminum pan and heated to 600 °C at a rate of 2 °C per minute under the flow of N_2. For defect testing, at least 10 mg of UiO-66 was loaded onto a tared aluminum pan and heated to 350 °C at a rate of 10 °C per minute and then held at 350 °C for 30 min under the flow of N_2 to ensure complete desolvation before cooling to 250 °C. Once at 250 °C, the sample was heated to 600 °C at a rate of 3 °C per minute under the flow of O_2 to combust organic ligand. Analogous to a previously reported method, the mass of the resulting ZrO_2 was compared to the mass of the desolvated MOF to calculate defectiveness.[29] Postcombustion analysis using UV−vis and IR spectroscopy confirmed that the product was composed solely of ZrO_2 (Figures S32 and S33).

DOI: 10.1021/acs.chemmater.9b01383
Chem. Mater. 2019, 31, 4831−4839

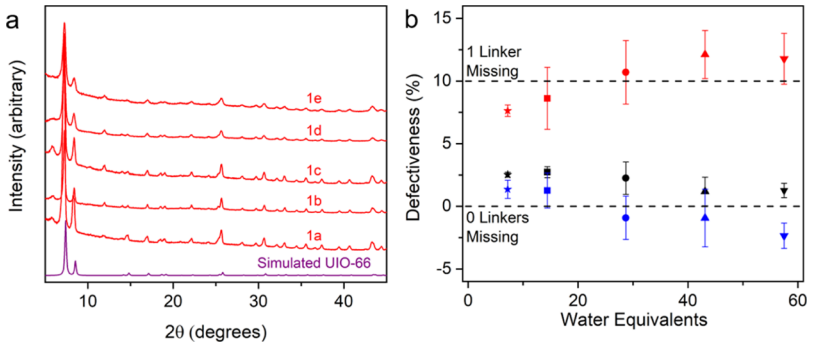

Figure 2. PXRD patterns and TGA defectiveness. (a) PXRD patterns of UiO-66 samples synthesized with a 1:1 L/M ratio (shown in red curves) and five different water contents [labeled (a–e) for 7.2–57.5 water equivalents]. (b) Plot of sample defectiveness as determined by TGA combustion with 1:1 L/M ratio samples in red, 1.5:1 L/M ratio samples in black, and 2:1 L/M ratio samples in blue. Mean ± SD are plotted from TGA defectiveness determinations on independently synthesized samples (n = 3).

NMR Digestions. In a 4 mL vial, 35 mg of CsF was dissolved in a mixture of 640 μL of DMSO-d_6 and 360 μL of D_2O. The clear solution was then added to a vial containing 5 mg of UiO-66 and sonicated for 5 min. The sample was then analyzed via ^{1}H NMR.

Concentration Determination. UiO-66 particle concentrations in dispersions were determined via TGA using a TA TGA 550. A known volume of dispersion had a DMF solvent evaporated via a heating ramp to 170 °C, leaving solid UiO-66 behind.

Dynamic Light Scattering. Dynamic light scattering (DLS) was performed using a Malvern Zetasizer Nano S. UiO-66 samples were prepared for DLS measurement by washing the as-synthesized samples in DMF to ensure removal of unreacted terephthalic acid (H_2bdc). Washing was performed by spinning down the as-synthesized UiO-66 nanoparticles and then redispersing them into DMF three times. The samples were then diluted to a concentration of 0.1 mg/mL, and their hydrodynamic diameters (D_h) and polydispersity indices (PDIs) were determined via DLS. Reported measurements are averages taken from three independently synthesized samples at the same synthetic conditions.

Sizing Using Scanning Electron Microscopy. Scanning electron microscopy (SEM) was performed using a JSM F7400 scanning electron microscope following sputter coating using a Denton Desk IV sputter coater. UiO-66 nanoparticle samples were prepared for imaging with SEM by solvent evaporation onto a glass slide, followed by gold/palladium sputter coating of ~5 nm. Following imaging, particle sizes were determined using the ImageJ program to manually size a selection of at least 50 particle diameters. The average of the particle measurements is denoted the geometric diameter of the sample.

Fluorescence Emission Studies. Fluorescence emission studies were performed using a BioTek Cytation 5 fluorescence microscope and a plate reader. UiO-66 nanoparticle samples were diluted to 0.5 mg/mL in water following three washes. Using a black-walled 96-well UV transparent plate, respective UiO-66 samples were excited at 280 nm, and the fluorescence emission was recorded from 300 to 550 nm.

Statistical Analysis. Statistical analysis of DLS and SEM particle sizing results was performed using a two-way analysis of variance (ANOVA) with the GraphPad Prism 7 software. This software was also used to perform Tukey's multiple comparisons for the aforementioned sizing results. Factorial design and analysis of fluorescence data was performed using the Minitab 17 software.

RESULTS AND DISCUSSION

Addition of Water To Control UiO-66 Crystallinity, Defects, and Surface Area. To quantitatively investigate the importance of water on the crystallization of UiO-66, we utilized anhydrous DMF (confirmed via NMR in Figure S1) in acid-free syntheses and systematically incorporated known amounts of water into our reaction mixture. Beginning with anhydrous DMF, the reaction of $ZrCl_4$ with one equivalent of H_2bdc at 110 °C for 24 h yielded negligible amounts of the amorphous material. This was expected given the necessity of water for cluster formation. Further testing revealed that a synthesis utilizing a minimum of ~8 equiv of water (50 μL of H_2O for a 15 mL solution) yielded crystalline UiO-66 (Figure 2a, labeled as 1a). This crystallinity was also maintained for syntheses utilizing 10 and 20 mL of DMF (Figure S7), indicating that crystallinity is a function of water equivalents relative to zirconium.

Although the PXRD pattern of this material (sample 1a) confirms the high crystallinity of this sample, the presence of the symmetry-disallowed peak at ~6° 2θ suggests the presence of cluster defects in the framework and thus missing organic linkers. This was confirmed using TGA combustion; sample 1a's (red star) defectiveness was determined to be ~1 linker missing per formula unit (Figure 2b). The nature of the cluster defects of this framework was explored with NMR spectroscopy. The ^{1}H NMR spectrum of a digested sample indicated a complete lack of formate, which is commonly encountered in UiO-66 as a cluster capping unit in both ligand and cluster defective frameworks (Figure S34). Formate capping units are often present even when formic acid is not used as a modulator, as it forms over the course of the reaction from the decomposition of DMF. The lack of additional NMR-active species suggests that the capping species present in this cluster-defective material are likely bdc^{2-} or OH^- with energy-dispersive X-ray spectra indicating no presence of chlorine (Figure S13).[29]

After determining the minimum water content for which a consistently crystalline material could be produced, we began exploring the effect of excess water on crystallinity and defectiveness of UiO-66. We employed solvothermal conditions with increasing water content in the synthesis until a crystalline product could not be isolated. Up to 57.5 equiv (400 μL) of added water, the crystallinity of the material was maintained, as can be seen from the PXRD patterns in Figure 2a. At water contents greater than 57.5 equiv, the crystallinity of the resulting product was low and highly variable between trials. At 14.4, 28.7, and 43.1 equiv of water (100, 200, and 300 μL of water added, respectively), the broad, symmetry-disallowed peak present in the PXRD patterns again indicates the presence of cluster defects in these materials. Although this feature was missing in the highest water content trial, TGA combustion of these samples indicated a defectiveness of ~1 linker/formula unit with an increase in defectiveness with higher water content (shown by the red symbols in Figure 2b).

DOI: 10.1021/acs.chemmater.9b01383
Chem. Mater. 2019, 31, 4831–4839

Again, NMR digestion indicated the absence of formate in these samples regardless of number of water equiv (Figure S34), suggesting that although the frameworks display missing cluster defects, adjacent clusters remain capped with bdc^{2-} or hydroxide. These NMR results, in combination with PXRD and TGA results, suggest that NMR cannot be used in isolation to judge defectiveness in UiO-66 materials, as although no formate is present in the MOF as a capping anion, both TGA and PXRD indicate significant defectiveness. These results also indicate that water content plays a large role in the nature of the capping ligand in defective materials.

In an attempt to decrease the defectiveness of UiO-66 below the observed ∼1 missing linker/formula unit with these initial syntheses (red symbols in Figure 2b), we synthesized UiO-66 at increased L/M ratios. From the formula unit of the hydrated structure, $Zr_6O_4(OH)_4(BDC)_6$, the theoretical minimum L/M ratio required to form the defect-free framework is 1:1. Increasing the L/M ratio beyond this point consistently afforded a material that was essentially defect-free as judged from TGA combustion experiments (Figures S22−S31). At a 1.5:1 L/M ratio with the minimum amount of water to yield a solid material (∼8 equiv), the resulting highly crystalline solid contained less than 0.25 missing linkers/formula unit determined via TGA (black symbols in Figure 2b). At this L/M ratio, samples synthesized with higher water contents had consistently low TGA defectiveness at 0.27, 0.22, 0.12, and 0.13 missing linkers/formula unit for syntheses utilizing 14.4, 28.7, 43.1, and 57.5 equiv of water, respectively. Further increasing the L/M ratio to 2:1 afforded lower defect materials (blue symbols in Figure 2b). PXRD patterns indicate that the highest and lowest water content samples at both the 1.5:1 and 2:1 L/M ratios lack cluster defects, while the others may have low levels of cluster defects. This is corroborated by NMR spectra of the digested samples (Figure S36), which indicate that the samples are devoid of a formate capping unit from decomposed DMF.

Surface area analyses are also consistent with this interpretation. We observe surface areas with median BET values of 1272, 1107, and 1070 m^2/g for the 1:1, 1.5:1, and 2:1 L/M ratios, respectively (Figures S40−S42). These surface areas are approaching the value expected for a perfectly defect-free material (954 m^2/g).[24] Previously reported BET surface areas for UiO-66 range from ∼600 to 1800 m^2/g, with higher defectiveness associated with higher surface area.[23] In comparison to our materials, the reported 1800 m^2/g framework has a significantly greater surface area, as it is one of the most defective UiO-66 materials reported with nearly two missing linkers/formula unit, as opposed to the frameworks prepared by the routes described here, which have a maximum of ∼1 missing linker/formula unit. It should be noted that previous studies have suggested that the TGA method of determining defectiveness in UiO-66 is problematic and that the pore volume, as determined via N_2 adsorption at 77 K, should be used as an indicator of lack of defects in samples. Median pore volumes for the three L/M samples prepared here are 0.52, 0.46, and 0.47 cm^3/g for 1:1, 1.5:1, and 2:1, respectively, approaching the value expected for the defect-free material (0.43 cm^3/g) and in agreement with TGA and surface area results.

The connection of synthetic conditions to defectiveness in acid-free syntheses is one of the first of its kind and allows for tuning of defectiveness for desired applications on the range of 0−1 linker missing per formula unit. This unprecedented synthetic control will allow for tunable defect-related properties including surface area for gas adsorption and loading of cargo for drug delivery applications. However, the differences in these synthetic conditions do have other effects on the material, such as the size of the yielded particles, another factor which can influence the material's usefulness in its desired application.

Impact of Synthetic Conditions on UiO-66 Particle Size. To further characterize the explicit role of water and L/M ratio in UiO-66 synthesis, SEM was utilized to observe trends in size and to unambiguously determine the geometric diameters (D_g) for each synthetic condition. Figure 3 shows a panel of representative SEM images of the UiO-66 nanoparticles, which demonstrates a variation of particle size as a function of both water content (rows) and L/M ratio (columns). These trends in size are quantified and displayed graphically in Figure 4a, which shows D_g measurements as a function of water equivalents in series corresponding to the three different L/M ratios. As can be seen from the images in Figure 3 as well as from the D_g sizing data in Figure 4a, the largest nanoparticles were formed at 14.3 equiv of water for both the 1:1 and 1.5:1 L/M ratio syntheses (118.2 ± 18.1 and 87.8 ± 12.2 nm, respectively), whereas the nanoparticles synthesized at a 2:1 L/M ratio exhibited a maximum D_g at 7.2 equiv of water added (91.9 ± 21.0 nm). As a general trend, syntheses with higher water contents led to smaller particle sizes with a plateau in size beyond 42.8 equiv of water for all L/M ratios. A similar trend was observed for the three L/M ratios, with D_g decreasing as the L/M ratio increased. These trends suggest that both the water content and the L/M ratio

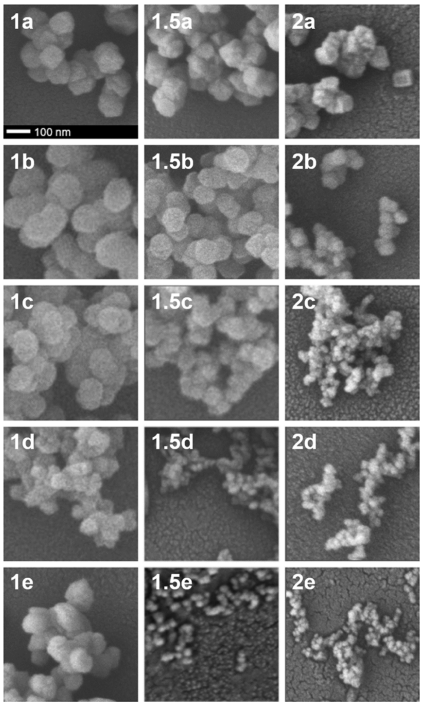

Figure 3. SEM images of UiO-66 nanoparticles. Representative SEM images used for the sizing of 15 samples across water addition and L/M ratios. Each column shows samples synthesized at different L/M ratios (1:1, 1.5:1, and 2:1, respectively). Each row indicates particles synthesized with increasing water content [(a) is 7.2 equiv of H_2O, (b) is 14.4 equiv, (c) is 28.7 equiv, (d) is 43.1 equiv, and (e) is 57.5 equiv]. The scale bar of 100 nm shown for 1a applies to all images.

DOI: 10.1021/acs.chemmater.9b01383
Chem. Mater. 2019, 31, 4831−4839

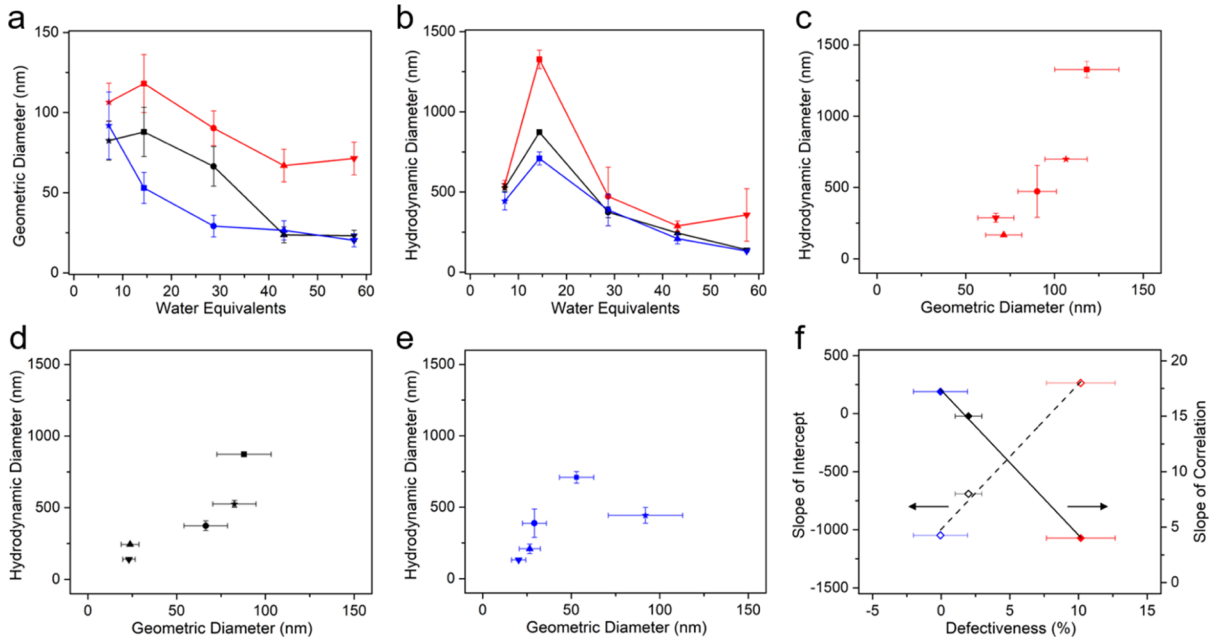

Figure 4. Defectiveness and particle sizing for UiO-66. For all plots, red, black, and blue represent 1:1, 1.5:1, and 2:1 L/M, respectively. (a) Geometric particle size measured via SEM as a function of water content. (b) Hydrodynamic diameter measured via DLS as a function of water content. (c) Hydrodynamic diameter vs geometric diameter for 1:1 L/M samples. Linear correlation yielded an R^2 value of 0.763. (d) Hydrodynamic diameter vs geometric diameter for 1.5:1 L/M samples. Linear correlation yielded an R^2 value of 0.774. (e) Hydrodynamic diameter vs geometric diameter for 2:1 L/M samples. Linear correlation yielded an R^2 value of 0.309. (f) Plot of correlations between geometric and hydrodynamic particle size as a function of defectiveness. Data in (a) are representative single values from repeated experiments. Data in (b) show mean ± SD for independently synthesized samples (n = 3).

have a significant impact on the particle D_g, which was confirmed via two-way ANOVA (see Table S7).

The D_g range achievable with the two simple modulators of water content and L/M ratio spans an order of magnitude and approaches the smallest reported size for UiO-66.[37,38] This is also the first reported synthesis of defect-free UiO-66 covering such a large particle size range (20.2 ± 4.0 to 91.9 ± 21.0 nm; see Table S5). Furthermore, this method of modulating defects and particle size, by tuning L/M ratio and water content, has not been utilized in previous reports for UiO-66 synthesis. The use of these modulators provides a new, facile synthetic handle for control of particle size while also affording consistently spherical, monodisperse, and nearly defect-free nanoparticles; features that have seldom been reported for syntheses without the use of acid as a modulator.[23]

Particle Sizing Correlations. As there is typically considerable cost and low throughput associated with SEM imaging, DLS was also used for particle size characterization. Figure 4b shows the hydrodynamic diameter (D_h) of the UiO-66 nanoparticles as measured via DLS. General trends observed with DLS sizing matched those for SEM sizing: D_h decreased both with an increased L/M ratio and increased water equivalents, and maximum D_h occurred at the same water content for all three L/M ratios, 14.4 equiv of water. However, the measured D_h were much greater than the measured D_g (see Table S5). Similar discrepancies between light scattering methods and geometric sizing methods have previously been reported, with the difference for MOF particles commonly attributed to aggregation.[23,26,37] However, intensity size distribution and low PDI results from light scattering measurements indicated that aggregation is not a factor for the UiO-66 nanoparticles (Figures S35−S49). This observation, coupled with the similar trends observed for the D_h and D_g measurements, led us to consider alternative sources of the discrepancy.

Size measurements made with DLS utilize the Stokes−Einstein equation to calculate z-averaged D_h, which reports the diameter of a hard sphere diffusing at an equivalent rate with the particles being measured.[39] This diameter equivalence will not necessarily be accurate for particles that are porous in nature, as drag both through and around the porous particles will impact rates of diffusion. This discrepancy has been reported previously for MOFs.[40] We hypothesized that elevated D_h measurements were linked to the degree of defectiveness, and thus porosity, of the particles, leading to the discrepancy between the two measurements (D_g and D_h). This was tested by plotting measured D_h and D_g for each L/M ratio, which have distinct defectiveness (Figure 4c−e). If a linear correlation between D_h and D_g is assumed, the slopes of the correlations (Figures S63−S65) between D_h and D_g increase with increasing nanoparticle defectiveness (and decreasing L/M ratio) as shown in Figure 4f. Thus, as D_g increases, higher defect nanoparticles will experience a greater relative increase in D_h than lower defect nanoparticles. This supports our hypothesis that increased defectiveness, and thus porosity, yield increased drag and result in overestimation of D_h from DLS. A similar comparison of the correlation intercepts shown in Figure 4f also yields a highly linear trend. Taken together, these correlations enable correction of D_h sizing to predict D_g using only defectiveness testing and link the role of increasing porosity on overestimated D_h sizing of MOF particles.

Particle Growth Kinetics Yield Decreased Defectiveness with Increased Size. In an effort to understand particle growth and defect development, time was also used as a modulator in a series of kinetic growth examinations from 15 min to 24 h using a subset of synthetic conditions (samples 1b

DOI: 10.1021/acs.chemmater.9b01383
Chem. Mater. 2019, 31, 4831−4839

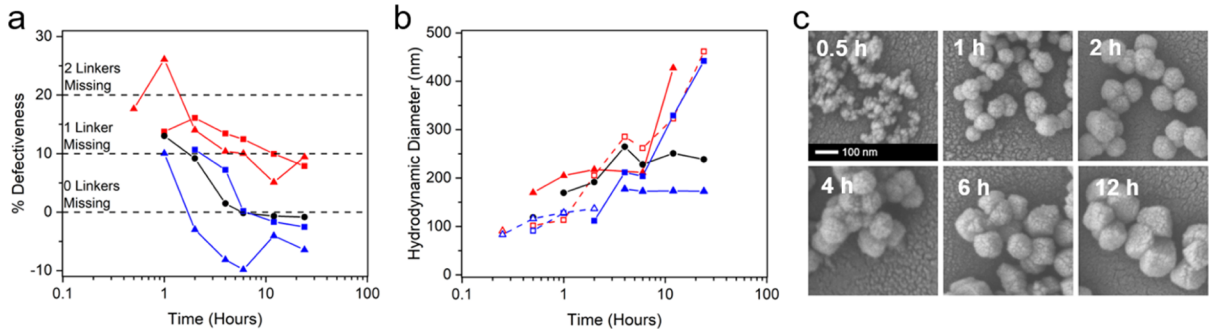

Figure 5. Defectiveness, particle size, and particle growth kinetics for UiO-66. For all plots, red, black, and blue represent 1:1, 1.5:1, and 2:1 L/M, respectively. (a) Plot of TGA defectiveness of samples 1b, 1d, 1.5c, 2b, and 2d over time. (b) Plot of D_h of samples 1b, 1d, 1.5c, 2b, and 2d over time as measured via DLS. Measurements made from isolated supernatants are shown with open symbols; those made from resuspended dry powders are shown in filled-in symbols. (c) Representative SEM images of sample 1b showing growth of the nanoparticles over time. Data in (a,b) are representative single values from repeated experiments.

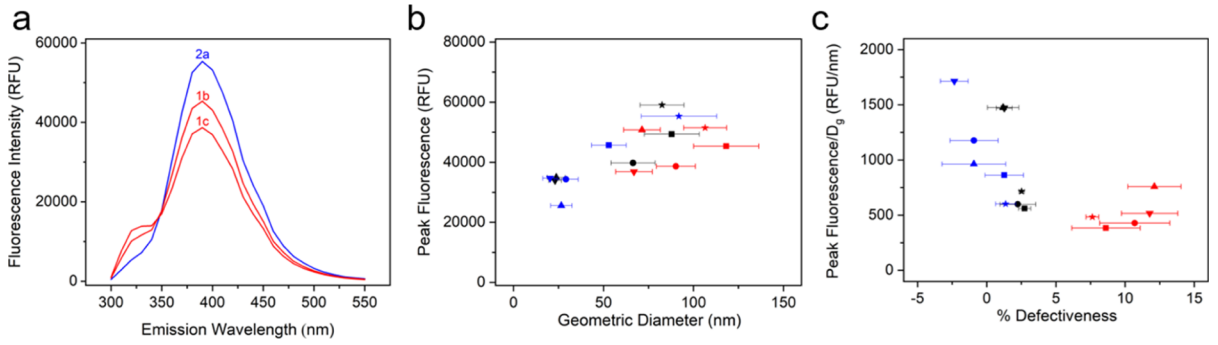

Figure 6. UiO-66 fluorescence and correlations. (a) Fluorescence emission spectra for UiO-66 samples 2a (blue star, D_g = 91.9 nm, 1.36% defective), 1b (red square, D_g = 66.8 nm, 12.11% defective), and 1c (red circle, D_g = 90.2 nm, 10.70% defective) following excitation at 280 nm. Peak emission is at 390 nm for all samples. (b) Plot of peak fluorescence vs D_g for all 15 samples. The general positive correlation between the two variables has an R^2 of 0.512. (c) Plot of peak fluorescence divided by D_g vs defectiveness for all 15 samples. The general negative correlation between the two variables has an R^2 of 0.442. Data in (b,c) plotted as mean ± SD (n = 3).

red square, 1d red triangle, 1.5c black circle, 2b blue square, and 2d blue triangle). These samples were chosen to explore the effects of time on particles with a variety of particle sizes, defectiveness, and synthetic conditions. As seen in Figure 5a, nanoparticle defectiveness generally decreased as a function of time for all five samples before reaching a plateau that corresponded to the reported defectiveness at 24 h (Figure 2b). Consistent with results for the full 24 h reactions, the 1:1 L/M ratio samples were the most defective materials across all time points. Samples that had previously been observed to be defect-free or nearly defect-free yielded 10% defective material (indicating 1 missing linker/formula unit) after just an hour of reaction time. Unlike the 1:1 L/M ratio samples, the nearly defect-free samples reached an observed plateau in defectiveness by the 6 h time point. This may indicate that the particle growth for these lower defect samples is completed earlier, which is similarly reflected in the particle sizing results for these samples (Figure 5b).

Measuring the size of UiO-66 kinetics samples synthesized at less than 1 h time points posed a challenge because of the lack of visible precipitates in the reaction vessel after initial centrifugation. To further test if there were nanoparticles forming in solution that were not visible (D_g less than 20 nm), the supernatants from the samples that reacted for less than 1 h were sedimented via ultracentrifugation. As this process successfully separated the remaining nanoparticles, this procedure was employed for all time points without visible precipitates to allow for particle sizing via DLS. Utilizing the isolated nanoparticles from supernatant suspensions allowed for detection of particles with D_h as small as 30 nm and monitoring of particle growth over time. Particle size changes over time are shown in Figure 5b, which demonstrates considerable particle growth over the 24 h study for all samples. Interestingly, samples 2d (blue triangle) and 1.5c (black circle) show arrested growth after the 4 h time point, reaching sizes similar to those observed for previous samples synthesized for 24 h. The three other samples, however, continue to grow over the entire 24 h timeframe, suggesting that larger particle diameters may be achievable with longer time points. SEM measurements (Figure 5c) corroborate the growth of monodisperse nanoparticles starting at 30 min for sample 1b (red square) with gradual growth in D_g occurring similar to that of D_h.

These results indicate that time, in addition to water content and L/M ratio, can be utilized to modulate both the particle size and defectiveness of UiO-66 nanoparticles, providing another facile synthetic handle to tune the aforementioned characteristics for desired applications. Furthermore, the results of the study for higher water content samples may indicate that the kinetics of particle growth and formation of defects are linked to and arrested by the amount of water in the solvent, potentially an important result in explaining the mechanism of the formation of this MOF.

DOI: 10.1021/acs.chemmater.9b01383
Chem. Mater. 2019, 31, 4831−4839

UiO-66 Fluorescence as a Function of Size and Defect. There have been previous reports of the fluorescence of UiO-66 with amine-functionalized bdc ligands (UiO-66-NH_2)[23,41,42] and for other bdc-containing MOFs;[43,44] however, fluorescence of UiO-66 has not previously been reported. Figure 6a shows representative fluorescence spectra of UiO-66 samples 1b (red square), 1c (red circle), and 2a (blue star) in water following excitation at 280 nm, demonstrating inherent fluorescence of the UiO-66 framework. The fluorescent peak observed at 380 nm corresponds to a similar peak emission wavelength reported for other bdc-containing MOFs, which typically exhibit emission maxima between 358 and 430 nm.[45,46]

As can be seen from representative spectra in Figure 6a, the magnitude of fluorescence intensity varied between UiO-66 samples. These representative spectra demonstrate the two general trends in fluorescence observed for UiO-66. First, as particle size increases, the maximum fluorescence intensity at constant mass concentration also increases. This trend is observed by comparing spectra from samples 1d (red triangle, D_g = 66.8 ± 10.2 nm, 12.11% defective) and 1c (red circle, D_g = 90.2 ± 10.9 nm, 10.70% defective), which have similar defectiveness but varied particle size. The trend in fluorescence with varying particle size can be seen more generally in Figure 6b, which demonstrates the positive correlation between peak fluorescence and D_g for all synthesized samples. Second, as the defectiveness of the nanoparticles is reduced, the maximum fluorescence intensity at constant mass concentration increases. This trend is observed by comparing the spectra from samples 1c (red circle, D_g = 90.2 nm, 10.70% defective) and 2a (blue star, D_g = 91.9 ± 21.0 nm, 1.36% defective), which have similar particle sizes but varied defectiveness. By decoupling the role of particle size from fluorescence intensity, Figure 6c demonstrates that fluorescence scaled by D_g is negatively correlated with defectiveness. Thus, lower defect nanoparticles exhibit greater maximum fluorescence intensities than higher defect nanoparticles.

Comparable to other MOFs based on bdc^{2-} ligands, fluorescence in UiO-66 is likely either a result of either ligand-to-metal charge transfer (LMCT) or ligand-based fluorescence.[47] Lower defect particles, which would have more ligand per formula unit and thus more sites for LMCT or linker-based fluorescence, would be expected to have greater fluorescence after decoupling other effects such as size. This trend was further explored through the implementation of a factorial analysis of the nanoparticle fluorescence (see Table S12), which confirms this result and indicates that the fluorescence is also a function of the interaction between D_g and defectiveness. This is the first report of the inherent fluorescence of nonfunctionalized UiO-66 and also connects peak nanoparticle fluorescence to both particle size and defectiveness, confirming the hypothesis that lower defect nanoparticles have greater peak fluorescence relative to higher defect nanoparticles.

CONCLUSIONS

We have devised a facile approach to tune the physical characteristics of UiO-66 nanoparticles using water content, L/M ratio, and reaction time as modulators. Modulation of water content and addition of ligand beyond the stoichiometric requirement during synthesis yielded tunable control of highly monodisperse UiO-66 nanoparticles on a geometric size range of 20−120 nm. These modulators also afforded significant control over framework defectiveness, which was observed to decrease over time during particle growth. Simultaneous control over the combination of nanoparticle sizes and defectiveness has not previously been reported for UiO-66. Accordingly, this work represents the first step toward application-specific tuning of these parameters, as both factors have effects on gas storage and drug delivery, as smaller, more defective nanoparticles typically have higher gas adsorption capacities and particle uptake is dependent on particle size. We also report that nanoparticle defectiveness is linked to common overestimation in DLS particle sizing and have determined a correlation to correct elevated values of D_h using TGA quantification of defectiveness. Finally, we report inherent fluorescence of nonfunctionalized UiO-66, which exhibits peak fluorescence at a wavelength of 390 nm following excitation at 280 nm and is maximized in large, defect-free nanoparticles. The fluorescence of nonfunctionalized UiO-66 may enable utilization of these nanoparticles as fluorescent probes. Overall, this synthetic approach and characterization of defect, size, and fluorescence represent new opportunities to tune the physiochemical properties of UiO-66 frameworks for a wide range of applications in gas storage, membranes, and drug delivery.

ASSOCIATED CONTENT

Supporting Information

The Supporting Information is available free of charge on the ACS Publications website at DOI: 10.1021/acs.chemmater.9b01383.

Detailed experimental procedures, PXRD patterns, TGA and NMR data, SEM images, statistical analyses, 77 K N_2 adsorption isotherms, and fluorescence spectra (PDF)

AUTHOR INFORMATION

Corresponding Authors

*E-mail: cfromen@udel.edu (C.A.F.).
*E-mail: edb@udel.edu (E.D.B.).

ORCID

Catherine A. Fromen: 0000-0002-7528-0997
Eric D. Bloch: 0000-0003-4507-6247

Author Contributions

§G.E.D. and Z.S. authors contributed equally.

Funding

Research reported in this publication was supported by National Institutes of Health under award number P20GM104316. The content is solely the responsibility of the authors and does not necessarily represent the official views of the National Institutes of Health. This research used resources of the Advanced Photon Source, a U.S. Department of Energy (DOE) Office of Science User Facility operated for the DOE Office of Science by Argonne National Laboratory under contract no. DE-AC0206CH11357. We thank the Delaware Space Grant College and Fellowship Program (NASA Grant NNX15AI19H) for support of L.A.

Notes

The authors declare no competing financial interest.

DOI: 10.1021/acs.chemmater.9b01383
Chem. Mater. 2019, 31, 4831−4839

■ ACKNOWLEDGMENTS

We thank Benjamin A. Trump and the staff at 17-BM for assistance with diffraction experiments at Argonne National Laboratory.

■ REFERENCES

(1) Sumida, K.; Rogow, D. L.; Mason, J. A.; McDonald, T. M.; Bloch, E. D.; Herm, Z. R.; Bae, T.-H.; Long, J. R. Carbon Dioxide Capture in Metal−Organic Frameworks. *Chem. Rev.* **2012**, *112*, 724−781.

(2) Getman, R. B.; Bae, Y.-S.; Wilmer, C. E.; Snurr, R. Q. Review and Analysis of Molecular Simulations of Methane, Hydrogen, and Acetylene Storage in Metal−Organic Frameworks. *Chem. Rev.* **2012**, *112*, 703−723.

(3) Herm, Z. R.; Bloch, E. D.; Long, J. R. Hydrocarbon Separations in Metal−Organic Frameworks. *Chem. Mater.* **2014**, *26*, 323−338.

(4) Li, J.-R.; Kuppler, R. J.; Zhou, H.-C. Selective Gas Adsorption and Separation in Metal−Organic Frameworks. *Chem. Soc. Rev.* **2009**, *38*, 1477−1504.

(5) Furukawa, H.; Cordova, K. E.; O'Keeffe, M.; Yaghi, O. M. The Chemistry and Applications of Metal-Organic Frameworks. *Science* **2013**, *341*, 1230444.

(6) Wang, H.; Dong, X.; Lin, J.; Teat, S. J.; Jensen, S.; Cure, J.; Alexandrov, E. V.; Xia, Q.; Tan, K.; Wang, Q.; et al. Topologically Guided Tuning of Zr-MOF Pore Structures for Highly Selective Separation of C_6 Alkane Isomers. *Nat. Commun.* **2018**, *9*, 1745.

(7) Liu, J.; Chen, L.; Cui, H.; Zhang, J.; Zhang, L.; Su, C.-Y. Applications of Metal−Organic Frameworks in Heterogeneous Supramolecular Catalysis. *Chem. Soc. Rev.* **2014**, *43*, 6011−6061.

(8) Zheng, Y.; Zheng, S.; Xue, H.; Pang, H. Metal−Organic Frameworks for Lithium−Sulfur Batteries. *J. Mater. Chem. A* **2019**, *7*, 3469−3491.

(9) Kreno, L. E.; Leong, K.; Farha, O. K.; Allendorf, M.; Van Duyne, R. P.; Hupp, J. T. Metal−Organic Framework Materials as Chemical Sensors. *Chem. Rev.* **2012**, *112*, 1105−1125.

(10) Huxford, R. C.; Della Rocca, J.; Lin, W. Metal−Organic Frameworks as Potential Drug Carriers. *Curr. Opin. Chem. Biol.* **2010**, *14*, 262−268.

(11) Crawford, D.; Casaban, J.; Haydon, R.; Giri, N.; McNally, T.; James, S. L. Synthesis by Extrusion: Continuous, Large-Scale Preparation of MOFs Using Little or No Solvent. *Chem. Sci.* **2015**, *6*, 1645−1649.

(12) Howarth, A. J.; Liu, Y.; Li, P.; Li, Z.; Wang, T. C.; Hupp, J. T.; Farha, O. K. Chemical, Thermal and Mechanical Stabilities of Metal−Organic Frameworks. *Nat. Rev. Mater.* **2016**, *1*, 15018.

(13) Tan, K.; Nijem, N.; Canepa, P.; Gong, Q.; Li, J.; Thonhauser, T.; Chabal, Y. J. Stability and Hydrolyzation of Metal-Organic Frameworks with Paddle-Wheel SBUs upon Hydration. *Chem. Mater.* **2012**, *24*, 3153−3167.

(14) Moosavi, S. M.; Boyd, P. G.; Sarkisov, L.; Smit, B. Improving the Mechanical Stability of Metal−Organic Frameworks Using Chemical Caryatids. *ACS Cent. Sci.* **2018**, *4*, 832−839.

(15) Burtch, N. C.; Jasuja, H.; Walton, K. S. Water Stability and Adsorption in Metal−Organic Frameworks. *Chem. Rev.* **2014**, *114*, 10575−10612.

(16) Yuan, S.; Qin, J.-S.; Lollar, C. T.; Zhou, H.-C. Stable Metal−Organic Frameworks with Group 4 Metals: Current Status and Trends. *ACS Cent. Sci.* **2018**, *4*, 440−450.

(17) Cavka, J. H.; Jakobsen, S.; Olsbye, U.; Guillou, N.; Lamberti, C.; Bordiga, S.; Lillerud, K. P. A New Zirconium Inorganic Building Brick Forming Metal-Organic Frameworks with Exceptional Stability. *J. Am. Chem. Soc.* **2008**, *130*, 13850−13851.

(18) DeCoste, J. B.; Peterson, G. W.; Jasuja, H.; Glover, T. G.; Huang, Y.-g.; Walton, K. S. Stability and Degradation Mechanisms of Metal−Organic Frameworks Containing the $Zr_6O_4(OH)_4$ Secondary Building Unit. *J. Mater. Chem. A* **2013**, *1*, 5642−5650.

(19) Kandiah, M.; Usseglio, S.; Svelle, S.; Olsbye, U.; Lillerud, K. P.; Tilset, M. Post-Synthetic Modification of the Metal−Organic Framework Compound UiO-66. *J. Mater. Chem.* **2010**, *20*, 9848−9851.

(20) Valenzano, L.; Civalleri, B.; Chavan, S.; Bordiga, S.; Nilsen, M. H.; Jakobsen, S.; Lillerud, K. P.; Lamberti, C. Disclosing the Complex Structure of UiO-66 Metal-Organic Framework: A Synergic Combination of Experiment and Theory. *Chem. Mater.* **2011**, *23*, 1700−1718.

(21) DeStefano, M. R.; Islamoglu, T.; Garibay, S. J.; Hupp, J. T.; Farha, O. K. Room-Temperature Synthesis of UiO-66 and Thermal Modulation of Densities of Defect Sites. *Chem. Mater.* **2017**, *29*, 1357−1361.

(22) Hajek, J.; Caratelli, C.; Demuynck, R.; De Wispelaere, K.; Vanduyfhuys, L.; Waroquier, M.; Van Speybroeck, V. On the Intrinsic Dynamic Nature of the Rigid UiO-66 Metal−Organic Framework. *Chem. Sci.* **2018**, *9*, 2723−2732.

(23) Schaate, A.; Roy, P.; Godt, A.; Lippke, J.; Waltz, F.; Wiebcke, M.; Behrens, P. Modulated Synthesis of Zr-Based Metal-Organic Frameworks: From Nano to Single Crystals. *Chem. - Eur. J.* **2011**, *17*, 6643−6651.

(24) Wu, H.; Chua, Y. S.; Krungleviciute, V.; Tyagi, M.; Chen, P.; Yildirim, T.; Zhou, W. Unusual and Highly Tunable Missing-Linker Defects in Zirconium Metal−Organic Framework UiO-66 and Their Important Effects on Gas Adsorption. *J. Am. Chem. Soc.* **2013**, *135*, 10525−10532.

(25) Chen, Q.; He, Q.; Lv, M.; Xu, Y.; Yang, H.; Liu, X.; Wei, F. Selective Adsorption of Cationic Dyes by UiO-66-NH_2. *Appl. Surf. Sci.* **2015**, *327*, 77−85.

(26) Morris, W.; Wang, S.; Cho, D.; Auyeung, E.; Li, P.; Farha, O. K.; Mirkin, C. A. Role of Modulators in Controlling the Colloidal Stability and Polydispersity of the UiO-66 Metal-Organic Framework. *ACS Appl. Mater. Interfaces* **2017**, *9*, 33413−33418.

(27) Wang, K.; Li, C.; Liang, Y.; Han, T.; Huang, H.; Yang, Q.; Liu, D.; Zhong, C. Rational Construction of Defects in a Metal−Organic Framework for Highly Efficient Adsorption and Separation of Dyes. *Chem. Eng. J.* **2016**, *289*, 486−493.

(28) Gutov, O. V.; Hevia, M. G.; Escudero-Adán, E. C.; Shafir, A. Metal−Organic Framework (MOF) Defects under Control: Insights into the Missing Linker Sites and Their Implication in the Reactivity of Zirconium-Based Frameworks. *Inorg. Chem.* **2015**, *54*, 8396−8400.

(29) Shearer, G. C.; Chavan, S.; Ethiraj, J.; Vitillo, J. G.; Svelle, S.; Olsbye, U.; Lamberti, C.; Bordiga, S.; Lillerud, K. P. Tuned to Perfection: Ironing out the Defects in Metal-Organic Framework UiO-66. *Chem. Mater.* **2014**, *26*, 4068−4071.

(30) Jiao, Y.; Liu, Y.; Zhu, G.; Hungerford, J. T.; Bhattacharyya, S.; Lively, R. P.; Sholl, D. S.; Walton, K. S. Heat-Treatment of Defective UiO-66 from Modulated Synthesis: Adsorption and Stability Studies. *J. Phys. Chem. C* **2017**, *121*, 23471−23479.

(31) Peterson, G. W.; Destefano, M. R.; Garibay, S. J.; Ploskonka, A.; McEntee, M.; Hall, M.; Karwacki, C. J.; Hupp, J. T.; Farha, O. K. Optimizing Toxic Chemical Removal through Defect-Induced UiO-66-NH_2 Metal−Organic Framework. *Chem.—Eur. J.* **2017**, *23*, 15913−15916.

(32) Rejman, J.; Oberle, V.; Zuhorn, I. S.; Hoekstra, D. Size-Dependent Internalization of Particles via the Pathways of Clathrin- and Caveolae-Mediated Endocytosis. *Biochem. J.* **2004**, *377*, 159−169.

(33) Butova, V. V.; Budnyk, A. P.; Charykov, K. M.; Vetlitsyna-Novikova, K. S.; Lamberti, C.; Soldatov, A. V. Water as a Structure-Driving Agent between the UiO-66 and MIL-140A Metal−Organic Frameworks. *Chem. Commun.* **2019**, *55*, 901−904.

(34) Ragon, F.; Horcajada, P.; Chevreau, H.; Hwang, Y. K.; Lee, U.-H.; Miller, S. R.; Devic, T.; Chang, J.-S.; Serre, C. In Situ Energy-Dispersive X-Ray Diffraction for the Synthesis Optimization and Scale-up of the Porous Zirconium Terephthalate UiO-66. *Inorg. Chem.* **2014**, *53*, 2491−2500.

(35) Atzori, C.; Shearer, G. C.; Maschio, L.; Civalleri, B.; Bonino, F.; Lamberti, C.; Svelle, S.; Lillerud, K. P.; Bordiga, S. Effect of Benzoic Acid as a Modulator in the Structure of UiO-66: An Experimental and Computational Study. *J. Phys. Chem. C* **2017**, *121*, 9312−9324.

DOI: 10.1021/acs.chemmater.9b01383
Chem. Mater. 2019, 31, 4831−4839

(36) Walton, K. S.; Snurr, R. Q. Applicability of the BET Method for Determining Surface Areas of Microporous Metal−Organic Frameworks. *J. Am. Chem. Soc.* **2007**, *129*, 8552−8556.
(37) Arcuri, C.; Monarca, L.; Ragonese, F.; Mecca, C.; Bruscoli, S.; Giovagnoli, S.; Donato, R.; Bereshchenko, O.; Fioretti, B.; Costantino, F. Probing Internalization Effects and Biocompatibility of Ultrasmall Zirconium Metal-Organic Frameworks UiO-66 NP in U251 Glioblastoma Cancer Cells. *Nanomaterials* **2018**, *8*, 867.
(38) Taddei, M.; Dümbgen, K. C.; Van Bokhoven, J. A.; Ranocchiari, M. Aging of the Reaction Mixture as a Tool to Modulate the Crystallite Size of UiO-66 into the Low Nanometer Range. *Chem. Commun.* **2016**, *52*, 6411−6414.
(39) Carvalho, P. M.; Felício, M. R.; Santos, N. C.; Gonçalves, S.; Domingues, M. M. Application of Light Scattering Techniques to Nanoparticle Characterization and Development. *Front. Chem.* **2018**, *6*, 237.
(40) Hirschle, P.; Preiß, T.; Auras, F.; Pick, A.; Völkner, J.; Valdepérez, D.; Witte, G.; Parak, W. J.; Rädler, J. O.; Wuttke, S. Exploration of MOF Nanoparticle Sizes Using Various Physical Characterization Methods-Is What You Measure What You Get? *CrystEngComm* **2016**, *18*, 4359−4368.
(41) Desai, A. V.; Samanta, P.; Manna, B.; Ghosh, S. K. Aqueous Phase Nitric Oxide Detection by an Amine-Decorated Metal-Organic Framework. *Chem. Commun.* **2015**, *51*, 6111−6114.
(42) Gao, X.; Cui, R.; Ji, G.; Liu, Z. Size and Surface Controllable Metal-Organic Frameworks (MOFs) for Fluorescence Imaging and Cancer Therapy. *Nanoscale* **2018**, *10*, 6205−6211.
(43) Li, Z.-Q.; Qiu, L.-G.; Wang, W.; Xu, T.; Wu, Y.; Jiang, X. Fabrication of Nanosheets of a Fluorescent Metal-Organic Framework $[Zn(BDC)(H_2O)]_n$ (BDC = 1,4-Benzenedicarboxylate): Ultrasonic Synthesis and Sensing of Ethylamine. *Inorg. Chem. Commun.* **2008**, *11*, 1375−1377.
(44) Dai, J.-C.; Wu, X.-T.; Fu, Z.-Y.; Hu, S.-M.; Du, W.-X.; Cui, C.-P.; Wu, L.-M.; Zhang, H.-H.; Sun, R.-Q. A Novel Ribbon-Candy-like Supramolecular Architecture of Cadmium(II)-Terephthalate Polymer with Giant Rhombic Channels: Twofold Interpenetration of the 3D $8^2$10-a Net. *Chem. Commun.* **2002**, *2*, 12−13.
(45) Fang, Q.; Zhu, G.; Shi, X.; Wu, G.; Tian, G.; Wang, R.; Qiu, S. Synthesis, Structure and Fluorescence of a Novel Three-Dimensional Inorganic-Organic Hybrid Polymer Constructed from Trimetallic Clusters and Mixed Carboxylate Ligands. *J. Solid State Chem.* **2004**, *177*, 1060−1066.
(46) Chen, W.; Wang, J.-Y.; Chen, C.; Yue, Q.; Yuan, H.-M.; Chen, J.-S.; Wang, S.-N. Photoluminescent Metal-Organic Polymer Constructed from Trimetallic Clusters and Mixed Carboxylates. *Inorg. Chem.* **2003**, *42*, 944−946.
(47) Allendorf, M. D.; Bauer, C. A.; Bhakta, R. K.; Houk, R. J. T. Luminescent Metal-Organic Frameworks. *Chem. Soc. Rev.* **2009**, *38*, 1330−1352.

DOI: 10.1021/acs.chemmater.9b01383
Chem. Mater. 2019, 31, 4831−4839